Contents lists available at ScienceDirect

Applied Catalysis B: Environment and Energy

Anchoring highly surface-exposed Pt single atoms on Ni_3S_2/Co_9S_8 with abundant S vacancies triggers *d*-orbital electron rearrangements for boosted seawater hydrogen evolution

Shanpeng Li [a,b,c], Yuling Zhuo [a,b], Dong Liu [a,*], Hui Pan [c,*], Zhenbo Wang [a,d,**]

[a] *College of Materials Science and Engineering, Shenzhen University, Shenzhen 518071, China*
[b] *College of Physics and Optoelectronic Engineering, Shenzhen University, Shenzhen 518060, China*
[c] *Institute of Applied Physics and Materials Engineering, University of Macau, Macao 999078, China*
[d] *MIIT Key Laboratory of Critical Materials Technology for New Energy Conversion and Storage, State Key Laboratory of Space Power-Sources, School of Chemistry and Chemical Engineering, Harbin Institute of Technology, Harbin 150001, China*

ARTICLE INFO

ABSTRACT

Improving the Pt atoms utilization efficiency on self-supported electrodes is crucial for industrial seawater hydrogen production, but effective strategies are still lacking. Herein, we reported a novel strategy to anchor highly surface-exposed Pt single atoms on Ni_3S_2/Co_9S_8 with abundant S vacancies ($Pt–Ni_3S_2/Co_9S_8–Sv$) as a self-supported electrode. Physical characterizations and theoretical calculations confirm that the strong Pt–S electron bridges with the coordinating role of surface S vacancies triggers the *d*-orbital electron rearrangements and regulates the local electron structures between the Co/Ni and Pt sites. Notably, the $Pt–Ni_3S_2/Co_9S_8–Sv$ electrode displays an ultralow overpotential of 18 mV at 10 mA cm^{-2} in alkaline seawater. More importantly, our $Pt–Ni_3S_2/Co_9S_8–Sv$ electrode assembled into an alkaline electrolysis cell can work continuously for 50 h under alkaline seawater @ 60 °C. This work provides a promising strategy for designing highly surface-exposed single-atomic catalyst for large-scale hydrogen evolution through seawater electrolysis.

1. Introduction

Seawater electrolysis is driven by renewable energy sources (i.e. wind, tidal, and solar energy), which are available over a large proportion of the Earth's surface; it is considered to be an inexpensive, sustainable and carbon-free approach to produce green hydrogen [1,2]. However, one of the main challenges of seawater electrolysis is the slow hydrogen evolution reaction (HER) kinetics [3,4]. In order to accelerate the HER kinetics, it is urgently required to develop low-cost, highly efficient, and robust catalysts. Although considerable efforts have been devoted to exploring non-precious metal-based catalysts, Pt-based catalysts are still the most effective HER catalysts owing to their high intrinsic activity and the excellent ability of Pt atoms to bond with hydrogen intermediates [5,6]. Unfortunately, due to the scarcity and elevated price of Pt, the large-scale preparation and industrial application of Pt-based catalysts are severely limited [7,8].

Pt single-atomic catalysts (SACs) are regarded as the most promising candidates for significantly enhancing the Pt atoms utilization efficiency [9,10]. However, Pt SACs still face many challenges when used in the seawater hydrogen evolution process. For instance, it is still unclear how the exposure of surface active centers can be increased and how suitable coordination bonds acting as fast electron transfer channels can be constructed [11–13]. Many studies have reported that anchoring highly dispersed Pt single atoms (SAs) on the substrate is an efficient strategy to enhance the HER activity through electronic metal–support interactions [14–17]. It is possible to induce charge transfer and rearrangement between the active metal and support to modulate the *d–p* orbital electrons of the active metal sites, thereby decreasing the adsorption free energy of the reaction intermediates to optimize the HER pathway [11, 18,19]. Recently, many transition metal sulfides (e.g., Ni_3S_2, CoS, and MoS_2) have been considered suitable for use as supports to anchor Pt SACs through the strong Pt–S bonds [20–22]. For example, M. A. et al. reported that the immobilization of Pt SAs on a CoS substrate (Pt@CoS) by means of the Pt–S bonds endows the material with a superior catalytic

---

performance with respect to that of commercial Pt/C, with a 45-fold increase in mass current density at 100 mV. Density functional theory (DFT) calculations revealed that the immobilized Pt SAs on the CoS interface result in an increased number of unhybridized d_{z^2} orbitals due to the interfacial synergy effect, which can significantly accelerate the dissociation kinetics of water [22]. In addition, Pt SACs with a stable coordination environment are beneficial for achieving an enhanced HER performance [15,16]. In this respect, defect engineering is widely believed to be a promising strategy to tune the local electron structures of active metal sites on the substrate surface [23–25]. For example, Chen and co-workers reported that the electron structures could be finely regulated through the incorporation of S vacancies in Co_3S_4; this approach can be used to modulate the surface binding energy of reaction intermediates and accelerate the electron migrations of adjacent atoms, thus enhancing the HER performance [26].

At the same time, the Pt SACs also face many challenges when used as large-scale electrodes in industrial electrolysis applications. The common synthesis method of Pt SACs is a high-temperature thermal reduction, which allows Pt atoms to aggregate easily and form Pt clusters or Pt nanoparticles instead of Pt SAs [27–29]. On the other hand, Pt SACs are mostly in powder form, and polymer binders, such as Nafion, need to be used during the large-scale preparation of industrial electrodes. This not only greatly reduces the actual utilization efficiency of Pt SACs, but also causes the catalyst to easily fall off from the electrode surface under high-current conditions [30–32]. Compared with high-temperature thermal reduction methods, a mild, low-energy-consumption preparation method could be more suitable for the industrial production Pt SACs as it would provide abundant Pt SAs on the substrate surface, which would enhance the atom utilization efficiency and reduce the mass transfer resistance [14,33]. For example, Pt SACs have been synthesized on the nickel foam (NF) substrate using an in-situ electrochemical deposition method. It is expected to achieve nearly 100 % atom utilization efficiency of Pt SAC electrodes can be achieved, and the peeling of catalyst caused by the fast bubble production on the surface of SAC electrodes during application of the electrolytic cells can be avoided [15,16]. Therefore, in-situ electrochemical deposition is an attractive method to prepare Pt SAC electrodes for industrial seawater electrolysis.

In this work, we developed a novel strategy for utilizing the strong Pt–S bonds to anchor the highly surface-exposed Pt SAs on Ni_3S_2/Co_9S_8 with abundant S vacancies ($Pt–Ni_3S_2/Co_9S_8–Sv$) using an electrochemical deposition method. The obtained $Pt–Ni_3S_2/Co_9S_8–Sv$ as a self-supported electrode exhibits ultralow overpotentials of 14 and 18 mV at the current density of 10 mA cm^{-2} for HER in 1 M KOH and 1 M KOH seawater, respectively. X-ray absorption spectroscopy and DFT calculations together confirm that: i) the highly surface-exposed Pt SAs anchored on Ni_3S_2/Co_9S_8 with abundant S vacancies triggers *d*-orbital electron rearrangements through the strong Pt–S electron bridges; ii) the coordinating role of S vacancies on the surface of $Pt–Ni_3S_2/Co_9S_8–Sv$ regulates local electron structures between the Co/Ni and Pt sites. These two features enhance the catalytic activity and stability of seawater electrolysis hydrogen production. Remarkably, the prepared matched (+) NF//Pt–Ni_3S_2/Co_9S_8–Sv (−) electrode exhibits a superior catalytic performance to that of industrial (+) NF//NiMo (−) electrode for a practical alkaline electrolysis cell (AEC) system. More importantly, our $Pt–Ni_3S_2/Co_9S_8–Sv$ electrode assembled into the AEC system achieves a good long-term stability under continuous operation for 50 h @ 100 mA cm^{-2} under simulated industrial seawater electrolysis conditions, showing a negligible potential drop compared with respect to the original voltage.

2. Experimental section

2.1. Chemicals and materials

Co(NO$_3$)$_2$•6 H$_2$O (99.99 %), Ni(NO$_3$)$_2$•6 H$_2$O (99.99 %), Urea (AR), NH$_4$F (99 %), Na$_2$S (99 %), K$_2$PtCl$_4$ (99.99 %), KOH (ACS) were purchased from Aladdin BioChem Co.,Ltd. Nickel foam (NF) and industrial NiMo electrode were bought from Kunshan Guang jiayuan Electronic Co., Ltd in China. 5 wt% Nafion solution and commercial 20 wt% Pt/C catalyst were obtained from Johnson Matthey Chemical Reagent Co. Ltd.

2.2. Preparation of Ni/Co precursor

The NF (2 × 4 cm^2) was washed ultrasonically with the acetone to remove the organic matter and the 3 M HCl to remove the oxide layer on the NF surface. Subsequently, the NiCo precursor was grown on the NF by a hydrothermal reaction. Typically, the pre-treated NF was immersed into the solution containing 0.045 M Ni(NO$_3$)$_2$•6 H$_2$O, 0.09 M Co (NO$_3$)$_2$•6 H$_2$O, 0.7 M urea and 0.54 M NH$_4$F, and reacted at 120 °C for 5 h. Additionally, the different ratios of Ni/Co precursor were prepared by adjusting the molar ratios of Ni(NO$_3$)$_2$•6 H$_2$O/Co(NO$_3$)$_2$•6 H$_2$O, and denoted as Ni precursor, Co precursor, and Ni/Co precursor (2:1, 1:1, 1:3), respectively.

2.3. Preparation of Ni$_3$S$_2$/Co$_9$S$_8$

The as-prepared Ni/Co precursor was subsequently immersed into 0.2 M Na$_2$S solution and reacted at 160 °C for 10 h. After naturally cooling down to room temperature, the obtained Ni$_3$S$_2$/Co$_9$S$_8$ electrode was washed with deionized water and dried at room temperature. Meanwhile, the different ratios of Ni/Co precursors in 2.2 were prepared by the same hydrothermal process, and denoted as Ni$_3$S$_2$, Co$_9$S$_8$, and Ni$_3$S$_2$/Co$_9$S$_8$ (2:1, 1:1, 1:3), respectively.

2.4. Preparation of Pt–Ni$_3$S$_2$/Co$_9$S$_8$–Sv

The as-prepared Ni$_3$S$_2$/Co$_9$S$_8$ (2 × 2 cm^2) as the work electrode (WE) was immersed into 2 × 10^{-4} M K$_2$PtCl$_4$ solution for the electrochemical deposition of Pt atoms. A standard three-electrode system was applied for the electrochemical reduction process. The saturated calomel electrode (SCE) with a salt bridge was applied to as the reference electrode (RE), a carbon rod was performed as the counter electrode (CE). Using cyclic voltammetry with the parameter settings: scanning potential (0 to −1.8 V), scanning rate (50 mV s^{-1}), and scanning cycles (50 cycles, with the reduction time of 4000 s). At last, the obtained Pt–Ni$_3$S$_2$/Co$_9$S$_8$–Sv electrode was washed with deionized water and dried in vacuum at room temperature. To verify the generation of abundant S vacancies on the surface of Pt–Ni$_3$S$_2$/Co$_9$S$_8$–Sv in the electrochemical deposition process, the scanning cycles were controllably adjusted to 10, 30, 75, and 100 cycles, with the corresponding reduction time of 800, 2400, 5600, and 8000 s, respectively. Meanwhile, the different Ni/Co ratios in Ni$_3$S$_2$/Co$_9$S$_8$ samples were prepared by electrodepositing in 0.2 mM of K$_2$PtCl$_4$ with reduction time of 4000 s. In addition, the concentration of K$_2$PtCl$_4$ was adjusted to 0.1, 0.3 and 0.4 mM, respectively.

2.5. Preparation of commercial Pt/C

8 mg of commercial 20 wt% Pt/C catalyst was ultrasound in the solution consisting of ethanol (485 μL), isopropanol (485 μL), and 5 wt % Nafion (30 μL) for 60 min. The obtained ink was evenly added to the NF (working area of 1 × 1 cm^2), and dried in vacuum at room temperature overnight.

2.6. Material characterizations

The morphological features of catalysts were characterized by using scanning electron microscopy (SEM, JSM 7401 F, Tokyo, Japan) and high-resolution transmission electron microscopy (HRTEM, JEOL JEM-F200, Hitachi, Japan). The high-angle annular dark-field scanning transmission electron microscopy (HAADF-STEM) images, the Energy

dispersive spectroscopy (EDS), and the element mappings of Pt SACs were obtained via a microscope (JEOL ARM-200) at 200 kV, which equipped with a probe spherical aberration corrector (AC-STEM, JEM-ARM200F). The element contents of Pt SACs were determined by inductively coupled plasma emission spectroscopy (ICP-OES, Agilent 720ES). The crystalline phases of catalysts were measured using Rigaku D X-ray diffraction (XRD), with the parameter settings of scan rate (5° min^{-1}) and scan angle (5–90°). The electron paramagnetic resonance (EPR, Bruker EMXplus-6/1) was used to detect the surface S vacancies in catalysts, with the measuring parameters: X-band CW-EPR, QM09, Room temperature, 2.97 mW, 9.64 GHz microwave frequency, 100 kHz modulation frequency. The element valence states of catalysts were detected on the X-ray photoelectron spectroscopy (XPS, Thermo Fisher Escalab). The X-ray absorption spectroscopy (XAS, PLS-II, Korea) was measured to analyze the X-ray absorption near-edge structure (XANES) of catalysts. The Fourier transformation of extended X-ray absorption fine structure (EXAFS) oscillations from *k* space to *R* space was achieved to obtain a radial distribution function. All data fitting was completed in the Artemis program.

2.7. Electrochemical measurements

The electrochemical measurements were performed in a standard three-electrode system (CHI 660E) consisting of the self-supported electrode (1 × 1 cm^2, working electrode), a graphite rod (counter electrode), and an Hg/HgO (reference electrode) in 1 M KOH (pH = 14.0) and 1 M KOH seawater (pH = 13.8) electrolytes, respectively, at room temperature. The seawater (pH = 8.1) was obtained from the location of South China Sea, Shenzhen. Linear sweep voltammetry (LSV) curves were tested at a scanning rate of 1 mV s^{-1} with an iR-compensation. All potentials reported in our work are referenced to a reversible hydrogen electrode (RHE) via the following Nernst equation [22]:

$$E_{(RHE)} = E_{(SCE)} + 0.243V + 0.059 \times pH \tag{1}$$

The measurement of electric double layer capacitances were carried out at different scan rates (5, 10, 15, 20, and 25 mV s^{-1}) with a non-faradaic potential region of 0.46–0.56 V vs. RHE. The electrochemical impedance spectroscopy (EIS) was tested with a scanning frequency

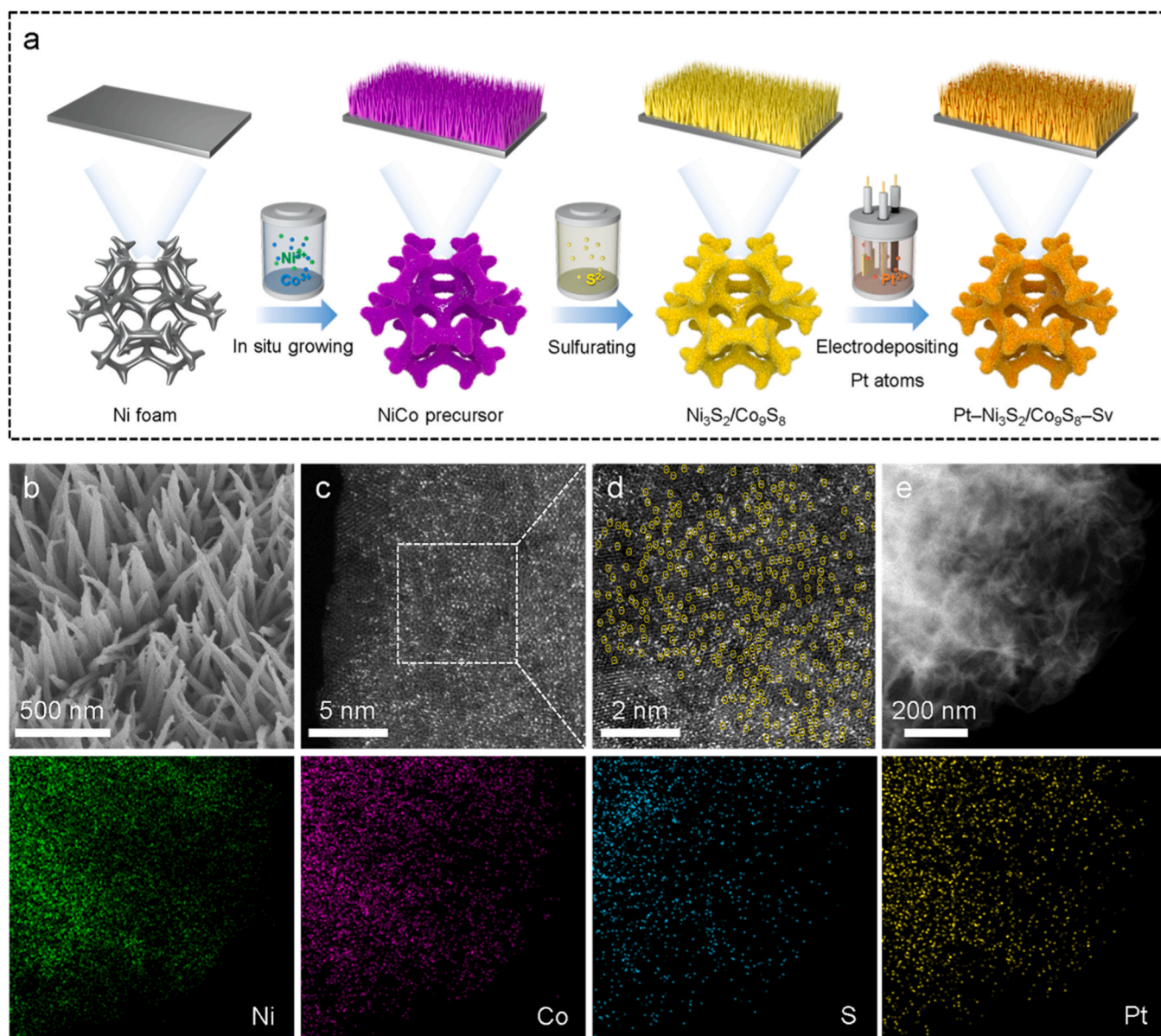**Fig. 1.** Schematic illustration and morphological characterization. (a) Schematic illustration showing the fabrication process of Pt–Ni$_3$S$_2$/Co$_9$S$_8$–Sv electrode. (b) SEM image, (c, d) HAADF-STEM images, and (e) Elemental mapping images of the Pt–Ni$_3$S$_2$/Co$_9$S$_8$–Sv.

range of 100 kHz to 0.01 Hz. The mass activity (MA) of Pt-based catalysts were calculated by the following equations[15]:

$$MA = \frac{j}{m_{Pt}} \qquad (2)$$

Here, j–current density (mA cm^{-2}) at a given overpotential, m_{Pt}–Pt mass loading, calculated by the determination result of ICP-OES.

Fig. 2. Physical characterization and coordination environment analysis. (a) XRD patterns of NF, Ni$_3$S$_2$/Co$_9$S$_8$/NF, and Pt–Ni$_3$S$_2$/Co$_9$S$_8$–Sv/NF. (b) EPR spectra of Ni$_3$S$_2$/Co$_9$S$_8$ and Pt–Ni$_3$S$_2$/Co$_9$S$_8$–Sv. (c) Pt 4f XPS spectrum of the Pt–Ni$_3$S$_2$/Co$_9$S$_8$–Sv/NF. (d) L$_3$-edge XANES of Pt in Pt–Ni$_3$S$_2$/Co$_9$S$_8$–Sv, Pt foil and PtO$_2$. The *inset* shows the average oxidation state of Pt in Pt–Ni$_3$S$_2$/Co$_9$S$_8$–Sv. (e) The corresponding k^3-weight FT-EXAFS of Pt in Pt–Ni$_3$S$_2$/Co$_9$S$_8$–Sv, PtS$_2$, Pt foil and PtO$_2$; (f) Wavelet transforms (WT) of Pt–Ni$_3$S$_2$/Co$_9$S$_8$–Sv, Pt foil and PtO$_2$. (g, h) Ni and Co K-edge XANES in Pt–Ni$_3$S$_2$/Co$_9$S$_8$–Sv and Ni$_3$S$_2$/Co$_9$S$_8$. (i, j) Ni and Co k^3-weight FT-EXAFS in Pt–Ni$_3$S$_2$/Co$_9$S$_8$–Sv, Ni$_3$S$_2$/Co$_9$S$_8$, Ni foil, and Co foil.

3. Results and discussions

3.1. Synthesis and structure characterization

Fig. 1a shows the synthetic process of Pt–Ni$_3$S$_2$/Co$_9$S$_8$–Sv. Firstly, the Ni/Co precursor was grown on the NF through a hydrothermal method (Figs. S1 and S2), and then a sulfuring process was carried out to obtain a self-supported Ni$_3$S$_2$/Co$_9$S$_8$ electrode (Fig. S3). After the hydrothermal process, Pt SAs were introduced into the as-prepared Ni$_3$S$_2$/Co$_9$S$_8$/NF for use as the cathode using a simple electrochemical deposition method. The morphology structures of pure NF, Ni/Co precursor/NF, and Ni$_3$S$_2$/Co$_9$S$_8$/NF nanoarrays are shown in Fig. S4. The scanning electron microscopy (SEM) image of the Pt–Ni$_3$S$_2$/Co$_9$S$_8$–Sv/NF (Fig. 1b) reveals the presence of wedge-shaped nanoarrays, which is consistent with the Ni$_3$S$_2$/Co$_9$S$_8$/NF. This indicates that the morphology structure of Ni$_3$S$_2$/Co$_9$S$_8$ could be maintained during the electrochemical deposition process without the presence of Pt nanoparticles. In order to confirm that the Pt SAs are anchored on the Ni$_3$S$_2$/Co$_9$S$_8$ with abundant S vacancies, high-angle annular dark-field scanning transmission electron microscopy (HAADF-STEM) was used, as shown in Fig. 1c, d. Numerous bright-contrast spots (yellow circles) are clearly observed, indicating that the ultrahigh atomic dispersed Pt SAs are uniformly exposed on the surface of Ni$_3$S$_2$/Co$_9$S$_8$ with abundant S vacancies. Moreover, the HAADF-STEM elemental mapping of Pt–Ni$_3$S$_2$/Co$_9$S$_8$–Sv clearly shows the homogeneous distribution of Ni, Co, S, and Pt elements (Fig. 1e). The corresponding energy-dispersive X-ray spectroscopy (EDS) analysis result shows that the atomic amount of Pt SAs reaches approximately 2.1 at% (Fig. S5). Furthermore, the determination results of ICP-OES reveal that: the mass amount of Pt SAs in Pt–Ni$_3$S$_2$/Co$_9$S$_8$–Sv was about 1.4 wt%; and the molar ratios of Ni/Co in Ni$_3$S$_2$/Co$_9$S$_8$ and Pt–Ni$_3$S$_2$/Co$_9$S$_8$–Sv were both close to 1:2 (Table S1).

The crystal structures of the Pt–Ni$_3$S$_2$/Co$_9$S$_8$–Sv catalyst were studied via X-ray diffraction analysis (XRD, Fig. 2a). The XRD peaks located at 21.8°, 31.1°, 37.8°, 38.3°, 44.3°, 49.7°, 50.1°, 55.2°, 73.0°, and 77.9° are attributed to the (1 0 1), (1 1 0), (0 0 3), (0 2 1), (2 0 2), (1 1 3), (2 1 1), (1 0 4), (1 2 2), (2 1 4), and (4 0 1) facets of high crystalline hexagonal Ni$_3$S$_2$ (PDF No. 44–1418) [34]. The other XRD diffraction peaks located at 29.8°, 31.1°, 51.9°, 54.6°, 55.7°, and 73.3° are related to the (3 1 1), (2 2 2), (4 4 0), (5 3 1), (6 0 0), and (7 3 1) facets of high crystalline cubic Co$_9$S$_8$ (PDF No. 02–1459) [35]. In addition, the intense and sharp diffraction peaks located at 44.5°, 51.8°, and 76.4° indicate the presence of a metallic Ni phase (PDF No. 04–0850) originated from the NF substrate [36]. Similarly, no peak corresponding to metallic Pt was observed in Pt–Ni$_3$S$_2$/Co$_9$S$_8$–Sv/NF. Furthermore, high-resolution transmission electron microscopy (HRTEM) image was acquired to observe the lattice information of Ni$_3$S$_2$/Co$_9$S$_8$ (Fig. S6). The two lattice spacings of 0.24 and 0.29 nm are assigned to the (0 0 3) facet of Ni$_3$S$_2$ and the (2 2 2) facet of Co$_9$S$_8$, respectively. Moreover, there are a small number of defects can be observed in the partial HRTEM image of Pt–Ni$_3$S$_2$/Co$_9$S$_8$–Sv (Fig. S7), which is possible caused by the existence of S vacancies. Hence, the electron paramagnetic resonance (EPR) spectrum was performed, as shown in Fig. 2b. Remarkably, the strong S vacancy signal peak located at $g = 2.002$ reveals that the abundant S vacancies on the surface of Pt–Ni$_3$S$_2$/Co$_9$S$_8$–Sv was generated during the electrochemical deposition process. This result is benefit for transferring electrons to the metal active centers to enhance catalytic activity [25]. Moreover, the concentration of S vacancies on the surface of Pt–Ni$_3$S$_2$/Co$_9$S$_8$–Sv (RT = 4000 s) was measured to be 2.27×10^{-5} M by the quantitative EPR determination (Fig. S8, Table S2). Subsequently, the surface chemical composition and element valence states of Pt–Ni$_3$S$_2$/Co$_9$S$_8$–Sv/NF were characterized via X-ray photoelectron spectroscopy (XPS). As shown in Fig. 2c, the binding energies of the Pt $4f_{7/2}$ and $4f_{5/2}$ orbitals were found to be 72.2 and 75.8 eV, respectively, which are slightly different from those of metallic Pt^0 (around 71.0 and 74.0 eV, respectively) [37]. The positive shift in the binding energy of Pt indicates that electrons have transferred from Pt to Ni$_3$S$_2$/Co$_9$S$_8$–Sv,

resulting in the formation of Pt$^{\delta+}$ arising from the Pt–S bonds in Pt–Ni$_3$S$_2$/Co$_9$S$_8$–Sv [22,38]. Moreover, the effect of Pt SAs coupling with abundant S vacancies to the element valence states in Ni$_3$S$_2$/Co$_9$S$_8$/NF was further studied, and the results are shown in Fig. S9a, b. For Ni 2p, there are two peaks located at 855.6 and 873.3 eV, which are attributed to Ni^{2+} 2$p_{3/2}$ and Ni^{2+} 2$p_{1/2}$, respectively; these peaks are the typical peaks of the Ni–S bond [36]. For Co 2p, there are two peaks located at 780.8 and 796.2 eV, which are assigned to Co^{2+} 2$p_{3/2}$ and Co^{2+} 2$p_{1/2}$, respectively; these peaks indicate that the Co–S bond has formed [39]. Interestingly, the Ni 2p and Co 2p characteristic peaks exhibit shifts of ~0.4 and ~0.5 eV toward lower binding energies, respectively, suggesting that the electron cloud densities around the Ni and Co atoms of Pt–Ni$_3$S$_2$/Co$_9$S$_8$–Sv were increased [20,22]. The peaks of S 2p peaks located at 161.5 and 163.4 eV were associated with S^{2-} 2$p_{3/2}$ and S^{2-} 2$p_{1/2}$ in Co$_9$S$_8$, respectively [40,41]. The peaks at 162.5 and 164.3 eV are assigned to S^{2-} 2$p_{3/2}$ and S^{2-} 2$p_{1/2}$ in Ni$_3$S$_2$, respectively [34]. It is worth noting that a shifts of ~0.2 eV toward a lower binding energy occurs for Pt–Ni$_3$S$_2$/Co$_9$S$_8$–Sv/NF (Fig. S9c), probably due to the electrons transferred from the Pt atoms to S atoms through the strong Pt–S bonds [22].

Furthermore, the local coordination environments and hyperfine structures of the Pt, Ni, and Co atoms in Pt–Ni$_3$S$_2$/Co$_9$S$_8$–Sv and Ni$_3$S$_2$/Co$_9$S$_8$ were investigated by the X-ray absorption near-edge structure (XANES) and extended X-ray absorption fine structure (EXAFS). As exhibited in Fig. 2d, the Pt-XANES spectrum of Pt–Ni$_3$S$_2$/Co$_9$S$_8$–Sv appears an intense white line (WL) located between the Pt foil and PtO$_2$, suggesting the presence of partially oxidized Pt species (Pt$^{\delta+}$) in Pt–Ni$_3$S$_2$/Co$_9$S$_8$–Sv. This result reveals that there are fewer electrons in the Pt 5d orbital of Pt–Ni$_3$S$_2$/Co$_9$S$_8$–Sv than in that of the Pt foil, which is due to the partial electrons transfer from the Pt atoms to Ni/Co atoms through the strong Pt–S bonds [22]. Moreover, the valance of Pt$^{\delta+}$ in Pt–Ni$_3$S$_2$/Co$_9$S$_8$–Sv was estimated to be about 1.47 based on the WL intensity (inset of Fig. 2d). The k^3-weighted Fourier transform (FT) EXAFS of Pt–Ni$_3$S$_2$/Co$_9$S$_8$–Sv (Fig. 2e) only shows a prominent peak at 1.81 Å. It does not coincide with the Pt–Pt bond (2.52 Å) of the Pt foil and the Pt–O bond (1.56 Å) of PtO$_2$, but it is consistent with the Pt–S bond (1.82 Å) of PtS$_2$ [27]. This finding confirms that the highly surface-exposed Pt SAs were successfully anchored on Ni$_3$S$_2$/Co$_9$S$_8$ with abundant S vacancies through the strong Pt–S bond [42]. Besides, the wavelet transform (WT) of EXAFS spectra were performed to gain insight into the changes in the overall coordination environment by the resolution of R and k spaces. As shown in Fig. 2f, the WT contours reveals that the Pt foil (Pt–Pt coordination bond) and PtO$_2$ (Pt–O coordination bond) show maximum intensities focus on $k = 8.83$ Å^{-1} and $k = 5.48$ Å^{-1}, respectively. However, the WT contours intensity of the Pt–Ni$_3$S$_2$/Co$_9$S$_8$–Sv is maximum around at $k = 6.25$ Å^{-1}, indicating that the formation of Pt–S coordination bond after anchoring highly surface-exposed Pt SAs on the Ni$_3$S$_2$/Co$_9$S$_8$ with abundant S vacancies. Additionallly, the different oscillation profiles of the extended EXAFS analysis of the k^3-weighted $\chi(k)$ signals (Fig. S10) prove that the coordination environment of Pt SAs in Pt–Ni$_3$S$_2$/Co$_9$S$_8$–Sv is different from that of the Pt foil and PtO$_2$. Moreover, the coordination environments of Ni (Fig. 2g) and Co (Fig. 2h) in Pt–Ni$_3$S$_2$/Co$_9$S$_8$–Sv and Ni$_3$S$_2$/Co$_9$S$_8$ were further inspected, respectively. In the front edge region, the binding energies of Ni and Co in Pt–Ni$_3$S$_2$/Co$_9$S$_8$–Sv are lower than those in Ni$_3$S$_2$/Co$_9$S$_8$. More specifically, the FT k^3-weighted EXAES spectra of Pt–Ni$_3$S$_2$/Co$_9$S$_8$–Sv, Ni$_3$S$_2$/Co$_9$S$_8$, the Ni foil (Fig. 2i), and the Co foil (Fig. 2j) show that the bond lengths of Ni–S (1.50 Å) and Co–S (1.65 Å) in Pt–Ni$_3$S$_2$/Co$_9$S$_8$–Sv are respectively 0.3 and 0.4 Å shorter than those in Ni$_3$S$_2$/Co$_9$S$_8$. This indicates that anchoring the highly surface-exposed Pt SAs on Ni$_3$S$_2$/Co$_9$S$_8$ with abundant S vacancies is helpful to increase electron cloud densities of the Ni and Co atoms. Furthermore, the coordination environment was also investigated by recording the strongest peaks of Ni WT-EXAFS (Fig. S11) and Co WT-EXAFS (Fig. S12) in Pt–Ni$_3$S$_2$/Co$_9$S$_8$–Sv (6.3 and 6.4 Å^{-1}, respectively) and Ni$_3$S$_2$/Co$_9$S$_8$ (6.2 and 6.0 Å^{-1}, respectively). These differences in bond lengths are mainly

ascribed to the local strain effects resulting from different coordination environments [43]. Furthermore, the Ni-EXAFS and Co-EXAFS oscillating structures of the Pt–Ni$_3$S$_2$/Co$_9$S$_8$–Sv remains unchanged in contrast to those of the Ni$_3$S$_2$/Co$_9$S$_8$ (Figs. S13 and S14); this is also consistent with the XRD results. On the basis of these results, it can be demonstrated that the highly surface-exposed Pt SAs are successfully anchored on Ni$_3$S$_2$/Co$_9$S$_8$ with abundant S vacancies through the strong Pt–S bonds, which promotes electrons effectively transferring from the Pt SAs to Ni/Co sites, and thus giving rise to a beneficial metal-support interaction for boosting the intrinsic catalytic activity.

3.2. HER electrocatalysis measurement

The HER performances of as-prepared catalysts were tested in a typical three-electrode system. Under the alkaline water condition (1 M

KOH), the LSV curves (Fig. 3a, Fig. S15) show that our Pt–Ni$_3$S$_2$/Co$_9$S$_8$–Sv only required very low overpotentials (η) of 14 and 42 mV at current densities of 10 and 100 mA cm^{-2}, respectively, which are significantly lower than those required by Ni$_3$S$_2$/Co$_9$S$_8$ (151 and 243 mV, respectively), NF (254 and 396 mV, respectively), and the benchmark Pt/C (26 and 126 mV, respectively. Meanwhile, the LSV curves during HER recorded on the catalyst regulations about different Ni/Co ratios in Ni$_3$S$_2$/Co$_9$S$_8$ before and after loading Pt species were presented in Figs. S16 and S17, respectively. Besides, the HER performances of the control Pt–Ni$_3$S$_2$/Co$_9$S$_8$–Sv samples from different concentrations of K$_2$PtCl$_4$ in the electrochemical deposition process was shown in Fig. S18. Subsequently, the relevant Tafel slope was calculated to determine the intrinsic catalytic kinetics of the catalysts (Fig. 3b). Remarkably, Pt–Ni$_3$S$_2$/Co$_9$S$_8$–Sv has the smallest Tafel slope (34 mV dec^{-1}), which is three times lower than that of Ni$_3$S$_2$/Co$_9$S$_8$ (100 mV
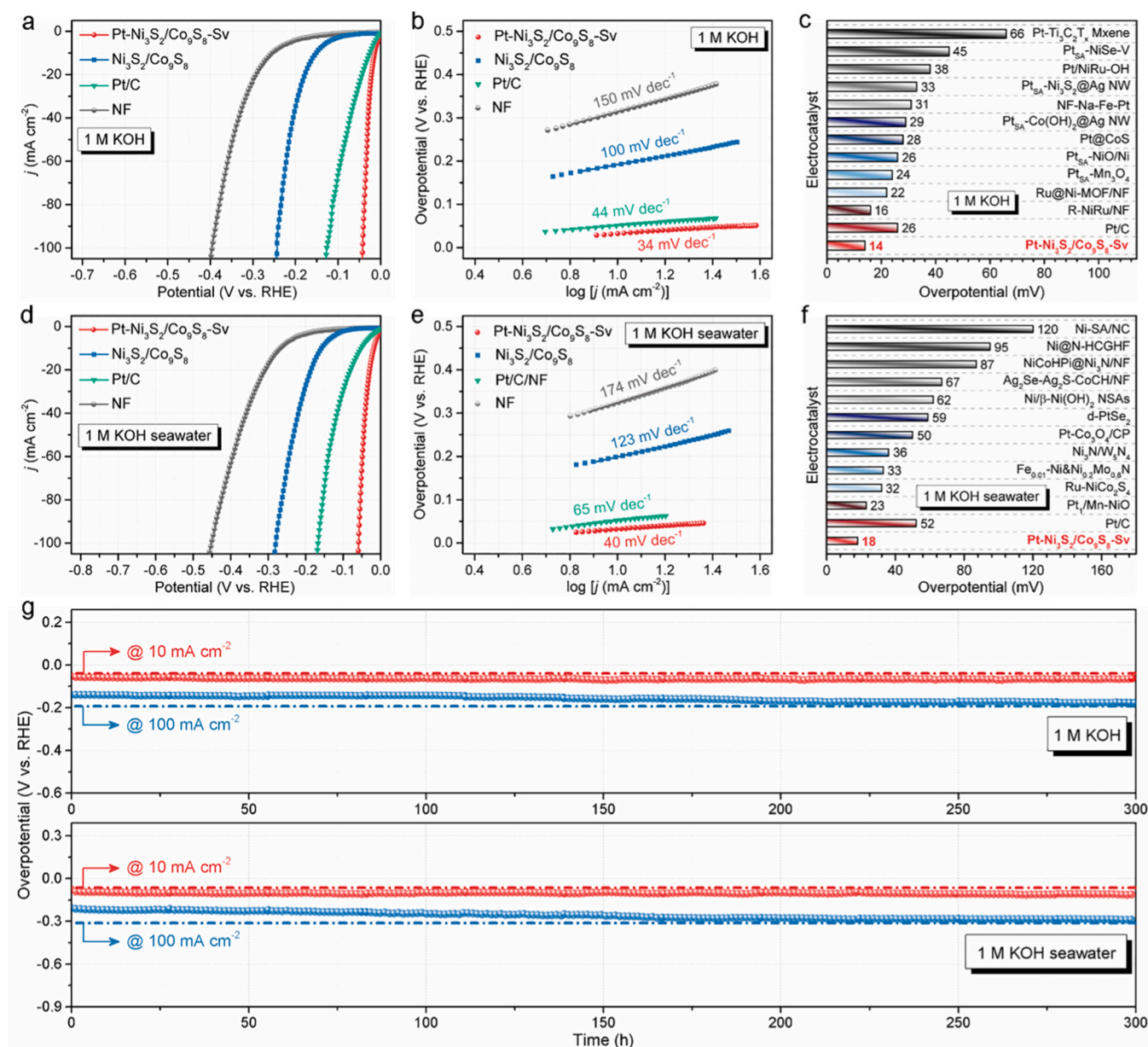

Fig. 3. HER performances. (a) LSV curves recorded on different electrodes in 1 M KOH electrolyte. (b) The relevant Tafel plots of the catalysts studied in a. (c) The comparisons of the overpotential at 10 mA cm^{-2} with the recently reported HER catalysts in 1 M KOH electrolyte. (d) LSV curves recorded on different electrodes in 1 M KOH seawater electrolyte. (e) The relevant Tafel plots of the catalysts studied in d. (f) The Comparisons of the overpotential at 10 mA cm^{-2} with the recently reported HER catalysts in 1 M KOH seawater electrolyte. (g) Chronopotentiometric curves recorded on the Pt–Ni$_3$S$_2$/Co$_9$S$_8$–Sv electrode at constant current densities of 10 and 100 mA cm^{-2} for HER in 1 M KOH and 1 M KOH seawater electrolytes, respectively.

dec^{-1}), and much smaller than that of the comparison catalysts, including the benchmark Pt/C (44 mV dec^{-1}). This indicates a higher transfer coefficient and a faster catalytic kinetics [44]. Moreover, the MA of Pt in Pt–Ni$_3$S$_2$/Co$_9$S$_8$–Sv reaches 1189 mA mg^{-1} @ 0.05 V in 1 M KOH (Fig. S19), which is 40 times higher than that of commercial Pt/C, indicating that anchoring highly surface-exposed Pt SAs on the Ni$_3$S$_2$/-Co$_9$S$_8$ with abundant S vacancies can remarkably improve the atom utilization efficiency of Pt and substantially reduce the cost of HER catalysts. To determine the original activity of Pt–Ni$_3$S$_2$/Co$_9$S$_8$–Sv, its electrochemically active surface area (ECSA) and electrochemical impedance spectroscopy (EIS) were subsequently evaluated. The ECSA is usually calculated to evaluate the number of active sites, which is proportional to the double-layer capacitance (C_{dl}) shown in Figs. S20 and S21. Owing to the hierarchical nanowire arrays, abundant S vacancies, and highly surface-exposed Pt SAs, the C_{dl} of Pt–Ni$_3$S$_2$/Co$_9$S$_8$–Sv (176.8 mF cm^{-2}) is larger than that of commercial Pt/C (129.7 mF cm^{-2}) and much larger than that of Ni$_3$S$_2$/Co$_9$S$_8$ (31.5 mF cm^{-2}) and NF (1.8 mF cm^{-2}). To probe the effects of the anchored Pt SAs on the interfacial charge transfer kinetics, EIS measurements were carried out in the range from 100 kHz to 0.01 Hz, and the fitted Nyquist plots and the equivalent circuit are shown in Fig. S22. Clearly, Pt–Ni$_3$S$_2$/Co$_9$S$_8$–Sv has a much lower charge-transfer resistance ($R_{ct} \approx 2.7 \; \Omega$) at the electrode–electrolyte interface than Pt/C ($R_{ct} \approx 7.6 \; \Omega$), Ni$_3S_2$/Co$_9S_8$ ($R_{ct} \approx 31.8 \; \Omega$), and NF ($R_{ct} \approx 94.7 \; \Omega$), indicating a faster electron transport toward the catalytic reaction. Notably, all results based on the analysis of the ECSA–C_{dl} and EIS–R_{ct} demonstrate that Pt–Ni$_3$S$_2$/Co$_9$S$_8$–Sv possesses an ultrahigh intrinsic HER activity.

On the other hand, seawater electrolytes have attracted increasing research interest owing to their abundant reserves, but there are currently very few SAC reported for use in seawater electrolysis for hydrogen production, especially regarding Pt SACs [13,45]. We also measured the hydrogen production performance of Pt–Ni$_3$S$_2$/Co$_9$S$_8$–Sv in alkaline seawater (Fig. 3d, Fig. S23). With respect to the LSV curves in 1 M KOH (Fig. 3a), it can be seen that the catalytic activity of Pt–Ni$_3$S$_2$/Co$_9$S$_8$–Sv in 1 M KOH seawater is lower slightly, which may be due to the decreases in conductivity in the complex seawater environment. Nonetheless, our Pt–Ni$_3$S$_2$/Co$_9$S$_8$–Sv catalyst retains an excellent HER activity in 1 M KOH seawater. Specifically, it only requires overpotentials of 18 and 59 mV to achieve current densities of 10 and 100 mA cm^{-2} in 1 M KOH seawater, respectively, and the relevant Tafel slope of Pt–Ni$_3$S$_2$/Co$_9$S$_8$–Sv in 1 M KOH seawater is only 40 mV dec^{-1} (Fig. 3e), which is close to the Tafel slope in 1 M KOH (34 mV dec^{-1}). Moreover, the MA of Pt in Pt–Ni$_3$S$_2$/Co$_9$S$_8$–Sv reaches 653 mA mg^{-1} at 0.05 V in 1 M KOH seawater, which is 49 times higher than that of benchmark Pt/C (Fig. S24), indicating that the highly surface-exposed Pt SAs was successfully anchored on Ni$_3$S$_2$/Co$_9$S$_8$ with abundant S vacancies can considerably broaden the application scope of Pt-based catalysts. Additionally, electrochemical characterizations, including ECSA–C_{dl} (Figs. S25 and S26) and EIS (Fig. S27) in a 1 M KOH seawater electrolyte, were conducted. These results prove that anchoring highly surface-exposed Pt SAs on the Ni$_3$S$_2$/Co$_9$S$_8$ with abundant S vacancies accelerates substantially HER kinetics in alkaline seawater, confirming its ability to almost completely adapt to the alkaline seawater environment and remain perfectly intact.

Such an efficient HER catalytic activity places the prepared Pt–Ni$_3$S$_2$/Co$_9$S$_8$–Sv catalyst among the best catalysts reported to date for hydrogen evolution in both alkaline water and seawater. Therefore, the Fig. 3c, f compare the overpotentials of Pt–Ni$_3$S$_2$/Co$_9$S$_8$–Sv at a current density of 10 mA cm^{-2} with that of the best reported SACs for both alkaline water and alkaline seawater hydrogen evolution, such as Pt$_1$/Mn–NiO [45], Pt$_{SA}$–NiO/NiO [46], Pt$_{SA}$–Mn$_3$O$_4$ [15], Pt$_{SA}$–NiSe–V [13], and Ru–NiCo$_2$S$_4$ [23]. It is found that our Pt–Ni$_3$S$_2$/Co$_9$S$_8$–Sv, which has a relatively low overpotential, is competitive compared with other SACs. More importantly, Pt–Ni$_3$S$_2$/Co$_9$S$_8$–Sv can be synthesized through a simple and controllable electrochemical deposition method, which is suitable for large-scale preparation, while the other listed SACs were

mainly synthesized through the high-temperature thermal reduction method (Tables S3 and S4). This suggested that our Pt–Ni$_3$S$_2$/Co$_9$S$_8$–Sv is more promising than other SACs for large-scale production.

The long-term stability of Pt–Ni$_3$S$_2$/Co$_9$S$_8$–Sv is another important factor affecting the hydrogen production when considering the practical application of this catalyst. However, the surface energy of SACs increasing sharply with the decrease in particle size during the electrons migration process [47,48], which results in these catalysts being stable for less than 100 h at a small current density (Table S5). To test the stability of our catalyst, the LSV curves were recorded before and after 10^4 CV cycles in both alkaline water/seawater electrolytes. As shown in Fig. S28, the LSV curves after CV cycling show slight declines in 1 M KOH and 1 M KOH seawater compared with the original curves. Meanwhile, the relevant plots of CV at its initial state and after 2000, 5000, and 10,000 cycles were shown in the *Inset* of Fig. S28, respectively. Fig. 3g illustrates the results of the long-term stability test of the Pt–Ni$_3$S$_2$/Co$_9$S$_8$–Sv catalyst at constant current densities in 1 M KOH and in 1 M KOH seawater electrolytes. It can be observed that over 300 h of continuous testing in 1 M KOH and 1 M KOH seawater electrolytes, the potential fluctuates only by 7 and 36 mV, respectively, which is probably due to the gas bubbles partially covering the active sites [49]. More importantly, the long-term stability test of the Pt–Ni$_3$S$_2$/Co$_9$S$_8$–Sv catalyst over 300 h in 1 M KOH seawater reveals that the potential increased by 16 and 65 mV at current densities of 10 and 100 mA cm^{-2}, respectively. To further assess the electrocatalytic durability of Pt–Ni$_3$S$_2$/Co$_9$S$_8$–Sv catalyst in alkaline seawater, the Multi-Current chronopotentiometric curve was measured, with a current density starting from 150 to 450 mA cm^{-2} with the increment of 50 mA cm^{-2} every 1000 s, as shown in Fig. S29, which revealed the outstanding mass transportation and electrical conductivity of the Pt–Ni$_3$S$_2$/Co$_9$S$_8$–Sv electrode due to the stable voltage produced as the current density increasing. Additionally, the chronopotentiometric curve recorded that the Pt–Ni$_3$S$_2$/Co$_9$S$_8$–Sv electrode could smoothly run under the industrial current density (400 mA cm^{-2}) for over 100 h (Fig. S30). These results demonstrate that the Pt–Ni$_3$S$_2$/Co$_9$S$_8$–Sv HER catalyst in a harsh seawater environment possesses an excellent corrosion resistance. Moreover, the structure stability of Pt–Ni$_3$S$_2$/Co$_9$S$_8$–Sv catalyst regarding its morphology and composition after prolonged HER testing was studied, and the results are presented in the Supplementary Material. The SEM images (Fig. S31) show that Pt–Ni$_3$S$_2$/Co$_9$S$_8$–Sv retained the intact nanoarrays structure except for the fact that part of the catalyst was detached after long-term operation for 13 days in alkaline water and alkaline seawater. The XRD (Fig. S32), XPS (Fig. S33), HAADF-STEM (Fig. S34), and EPR (Fig. S35), and results together show that the lattice phases, elemental valence states, surface-exposed Pt SAs, and abundant S vacancies in the Pt–Ni$_3$S$_2$/Co$_9$S$_8$–Sv catalyst maintain robust structures after testing for over 300 h in an alkaline seawater electrolytic environment.

3.3. Electrode industrial application

To assess the application prospects of our Pt–Ni$_3$S$_2$/Co$_9$S$_8$–Sv electrode in industrial AEC systems, Pt–Ni$_3$S$_2$/Co$_9$S$_8$–Sv and pure NF were used as the cathode and the anode in an AEC system, respectively, and operated in a simulated industrial seawater electrolysis environment. A schematic diagram of the AEC system and photographs of the experimental AEC devices and the amplified anodes/cathodes (4.5 × 4.5 cm^2) are shown in Fig. 4a and Fig. S36. Furthermore, an industrial NiMo electrode and a commercial Pt/C electrode were employed as cathodes for comparisons. The AEC system was operated in a simulated industrial electrolysis condition under 6 M KOH @ 60 °C and 6 M KOH seawater @ 60 °C, as shown in Fig. 4b, c. It can be clearly seen that the AEC operating voltage for (+) NF//Pt–Ni$_3$S$_2$/Co$_9$S$_8$–Sv (−) at a current density of 100 mA cm^{-2} was only 2.05 V in 6 M KOH @ 60 °C and 2.12 V in 6 M KOH seawater @ 60 °C, which are both lower than those of (+) NF//NiMo (−) (2.17 V in 6 M KOH @ 60 °C, and 2.21 V in 6 M KOH seawater
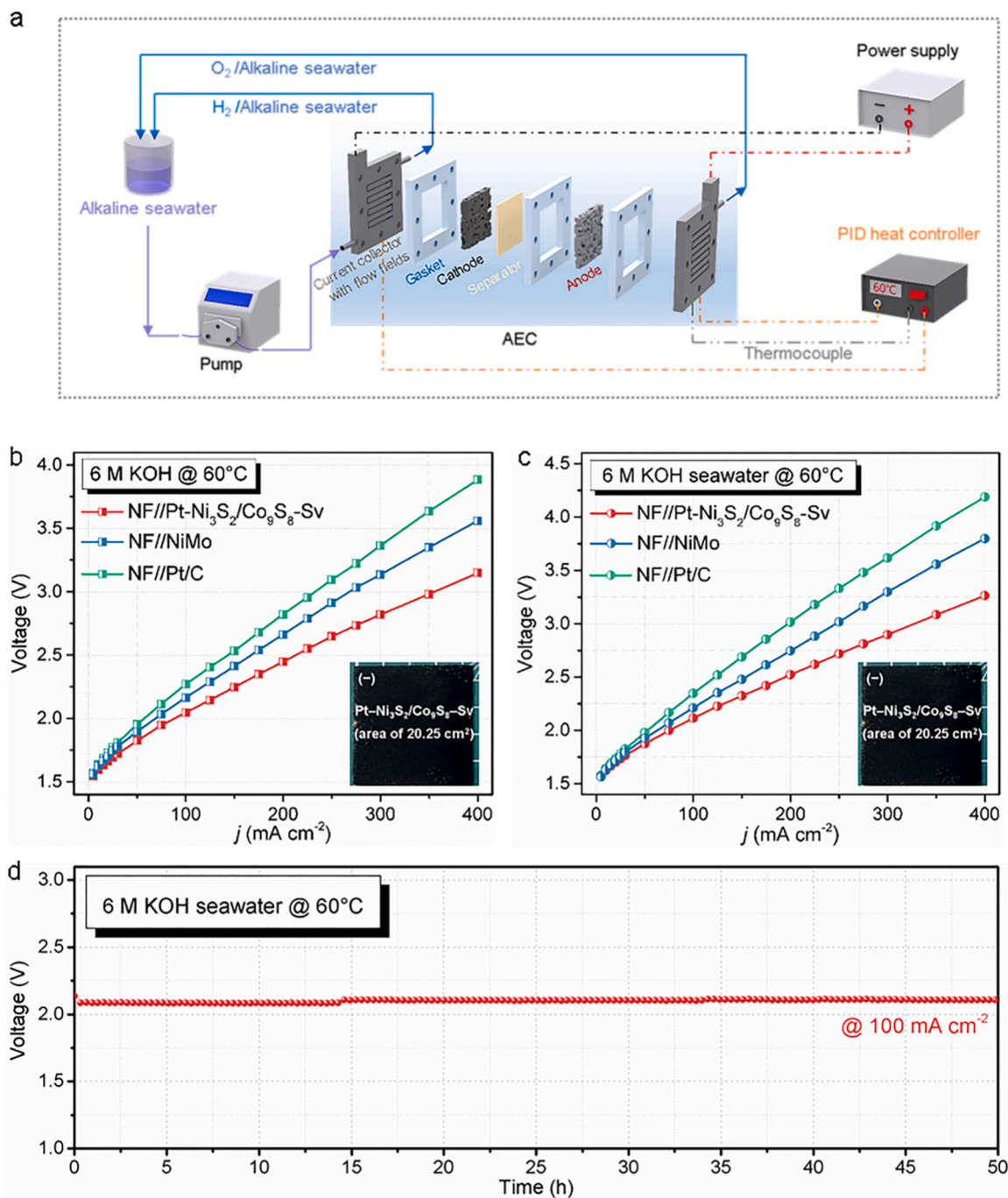
Fig. 4. Industrial application. (a) Schematic diagram of AEC device. (b, c) *I−V* curves of the AEC in 6 M KOH and 6 M KOH seawater @ 60 °C, respectively. (d) The durability test in the AEC with (+) NF//Pt–Ni$_3$S$_2$/Co$_9$S$_8$–Sv (−) in 6 M KOH seawater @ 60 °C.

@ 60 °C) and (+) NF//Pt/C (−) (2.27 V in 6 M KOH @ 60 °C, and 2.35 V in 6 M KOH seawater @ 60 °C). Additionally, the AEC system was analyzed in 1 M KOH and 1 M KOH seawater at room temperature. The AEC operating voltages of (+) NF//Pt–Ni$_3$S$_2$/Co$_9$S$_8$–Sv (−) were lower than those of (+) NF//NiMo (−) and (+) NF//Pt/C (−) (Fig. S37). More importantly, a durability test was conducted on the AEC system consisting of (+) NF//Pt–Ni$_3$S$_2$/Co$_9$S$_8$–Sv (−) in 6 M KOH seawater @ 60 °C (Fig. 4d). Notably, very little change in voltage can be observed during operation for 50 h at 100 mA cm^{-2}, which demonstrates the good durability of (+) NF//Pt–Ni$_3$S$_2$/Co$_9$S$_8$–Sv (−) in simulated industrial AEC systems. The above analysis proves that our Pt–Ni$_3$S$_2$/Co$_9$S$_8$–Sv has a great application prospect in industrial AEC system for seawater hydrogen evolution.

3.4. Insight into catalytic mechanism

Considering the HER catalytic active center for H$_2$O adsorption and dissociation steps was primarily selected at the transition metal sites [20,22], the Gibbs free energy of H$_2$O adsorption and dissociation at the Co/Ni sites of Pt–Ni$_3$S$_2$/Co$_9$S$_8$–Sv, Ni$_3$S$_2$/Co$_9$S$_8$, and simulated Ni$_3$S$_2$/Co$_9$S$_8$–Sv systems were initially assessed. Remarkably, as shown in Fig. 5a, the Co sites of Pt–Ni$_3$S$_2$/Co$_9$S$_8$–Sv has the lowest reaction energy barrier of H$_2$O adsorption and dissociation, including the adsorption free energy of H$_2$O ($\Delta G_{H_2O}^* = -1.379$), the transition-state free energy ($\Delta G_{TS1}^* = -0.988$, $\Delta G_{TS}^* = 0.378$), and the dissociation free energy of H$_2$O ($\Delta G_{OH+^*H}^* = -1.644$, $\Delta G_{OH+^*H_2}^* = -0.666$), respectively. This result suggests that the highly surface-exposed Pt SAs anchored on
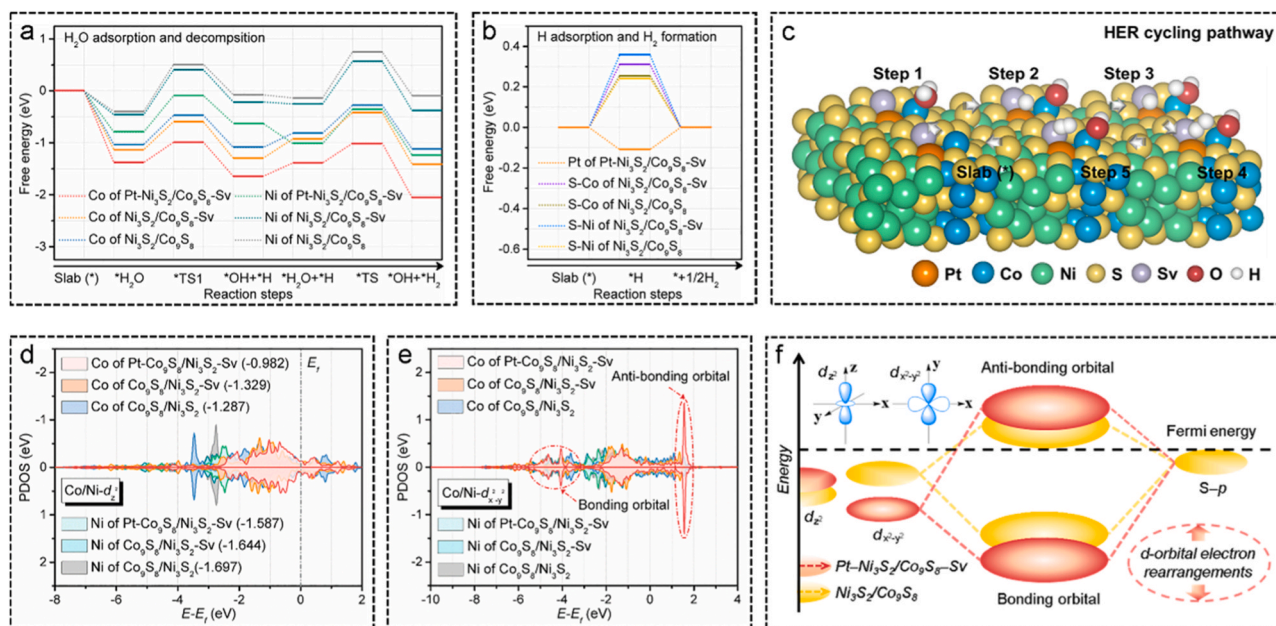
Fig. 5. Theoretical analysis of intrinsic catalytic activity. (a, b) Calculated free energy diagrams of the H_2O adsorption and decomposition at the Co/Ni sites, and the H adsorption and H_2 formation at the Pt or S sites in Pt–Ni_3S_2/Co_9S_8–Sv, Ni_3S_2/Co_9S_8, and simulated Ni_3S_2/Co_9S_8–Sv systems, respectively. (c) HER cycling pathway at the Co sites for H_2O dissociation and at the Pt sites for H_2 formation in Pt–Ni_3S_2/Co_9S_8–Sv. (d, e) Calculated projected density of states (PDOS) of Co/Ni–d_{z^2} and Co/Ni–$d_{x^2-y^2}$ in Pt–Ni_3S_2/Co_9S_8–Sv, Ni_3S_2/Co_9S_8, and simulated Ni_3S_2/Co_9S_8–Sv systems, respectively. (f) *d*-Orbital electron rearrangements schematic diagram in Pt–Ni_3S_2/Co_9S_8–Sv.

Ni_3S_2/Co_9S_8 with the coordination role of surface S vacancies promote the H_2O adsorption and dissociation at the Co/Ni sites. Besides, it was found that the Co sites possess the lower Gibbs free energy than the parallel Ni sites. Subsequently, Fig. 5b calculates the adsorption free energy of H at the Pt or S sites in above three systems, respectively. Unsurprisingly, the Pt sites of Pt–Ni_3S_2/Co_9S_8–Sv possess the lowest adsorption free energy of H (ΔG_{*H} = −0.109), which confirms that the Pt SAs is as the active metal sites for adsorbing H and forming H_2, which is also in agreement with previous results on Pt-based catalysts [6,15, 19]. Based on above calculated results, an optimal HER cycling pathway at the Co and Pt sites of Pt–Ni_3S_2/Co_9S_8–Sv is shown in Fig. 5c, mainly involving *H_2O (Step 1), *HO+*H (Step 2), *H_2O+*H (Step 3), *TS (Step 4), *HO+*H_2 (Step 5), and slab (*). More intuitively, the relationships between the Co/Ni-*d* band center and ΔG_{*H_2O}, ΔG_{*TS1}, and ΔG_{*TS} (Fig. S38); and the relationship between the Pt-*d* or S-*p* band center and ΔG_{*H} (Fig. S39) in above three systems forcefully demonstrated that the highly surface-exposed Pt SAs anchored on Ni_3S_2/Co_9S_8 with abundant S vacancies greatly lowers the energy barrier of H_2O dissociation at the Co/Ni sites and H_2 formation at the Pt sites. Meanwhile, the above calculated conclusions were well consistent with the experimental results recorded on the relevant LSV curves of Pt–Ni_3S_2/-Co_9S_8–Sv, Ni_3S_2/Co_9S_8, Co_9S_8, and Ni_3S_2 (Fig. S40).

To better elucidate the reaction mechanism, the projected density of states (PDOS) was determined and the local electron structures was analyzed in Pt–Ni_3S_2/Co_9S_8–Sv, Ni_3S_2/Co_9S_8, and simulated Ni_3S_2/Co_9S_8–Sv systems, which includes the Co/Ni–*d* orbitals for evaluating the ability to adsorb and decompose H_2O, and the Pt–*d* or S–*p* band centers are related to the formation of *H to H_2. It can be clearly observed that anchoring highly surfaced-exposed Pt SAs on the Ni_3S_2/Co_9S_8 with abundant S vacancies triggers the *d*-orbital electrons to rearrange. Specifically, the energy level of Co/Ni–d_{z^2} orbital in Pt–Ni_3S_2/Co_9S_8–Sv (−0.982 eV and −1.587 eV) is the closest the Fermi energy (Fig. 5d), which means that the best adsorption and decomposition ability to H_2O at the Co/Ni sites. Moreover, the energy levels of Co/Ni–$d_{x^2-y^2}$ bonding orbital and Co/Ni–$d_{x^2-y^2}$ anti-bonding orbital in Pt–Ni_3S_2/Co_9S_8–Sv increase considerably (Fig. 5e), which suggested

that the hybrid capacity of Co–S/Ni–S bond is enhanced and the length of Co–S/Ni–S bond is reduced, confirming the formation of a stable internal structure. Furthermore, the energy level of Pt–d_{z^2} orbital in Pt–Ni_3S_2/Co_9S_8–Sv (−3.122 eV) is the most appropriate to the adsorption of H (Figs. S41 and S42). Based on the calculated results, a *d*-orbital electron rearrangements schematic diagram is described in Fig. 5f. Anchoring the highly surface-exposed Pt SAs on Ni_3S_2/Co_9S_8 with abundant S vacancies enables that: i) The energy level of the unpaired d_{z^2} orbital on the vertical surface increases (becoming closer to the Fermi energy), which indicates an enhancement in the ability to adsorb and decompose H_2O; ii) The number of bonding orbital decreases as the hybridization of the $d_{x^2-y^2}$ orbital in the plane causes the Co–S/Ni–S bonds to become more stable and the Co–S/Ni–S bond length to become correspondingly shorter, which is well constant with the results of EXAFS. Moreover, as shown in Fig. S43, the local charges density changes were confirmed by electron cloud density difference maps of the Pt–Ni_3S_2/Co_9S_8–Sv comparing with simulated Ni_3S_2/Co_9S_8–Sv, and the simulated Ni_3S_2/Co_9S_8–Sv comparing with Ni_3S_2/Co_9S_8. Here, the yellow electron clouds represents electrons lost and the blue electron clouds means electrons gained, respectively. According to the electron cloud density distribution changes, this phenomenon is ascribed that the highly surface-exposed Pt SAs anchored on Ni_3S_2/Co_9S_8 with abundant S vacancies provides abundant electrons to Co/Ni sites via the strong Pt–S electron bridges, which triggers a beneficial rearrangement of *d*-orbital electrons, thus boosting the HER catalytic activity and seawater electrolytic stability. Besides, the coordination role of surface S vacancies in Pt–Ni_3S_2/Co_9S_8–Sv regulates the local electron structures between the Co/Ni and Pt sites.

4. Conclusion

In summary, we have demonstrated that the highly surface-exposed Pt SAs were successfully anchored on the Ni_3S_2/Co_9S_8 with abundant S vacancies (Pt–Ni_3S_2/Co_9S_8–Sv) for use as a self-supported electrode using an electrochemical deposition method. The obtained Pt–Ni_3S_2/ Co_9S_8–Sv electrode only requires overpotentials of 14 and 18 mV to

deliver 10 mA cm^{-2} in 1 M KOH and 1 M KOH seawater, respectively. Notably, the Pt–Ni$_3$S$_2$/Co$_9$S$_8$–Sv electrode shows a good long-term stability of 300 h at 100 mA cm^{-2} in both alkaline water and seawater electrolytes. More importantly, our Pt–Ni$_3$S$_2$/Co$_9$S$_8$–Sv electrode assembled into an AEC system was able to operate continuously for 50 h at a stable voltage of 2.1 V at 100 mA cm^{-2} in 6 M KOH seawater @ 60 °C, and its performance was superior to that the industrial NiMo electrode and commercial Pt/C electrode. Based on experimental characterizations and DFT calculations, the excellent HER performances of Pt–Ni$_3$S$_2$/Co$_9$S$_8$–Sv electrode in both alkaline water/seawater environments can be ascribed as follows: i) the highly surface-exposed Pt SAs anchored on Ni$_3$S$_2$/Co$_9$S$_8$ with abundant S vacancies triggers *d*-orbital electron rearrangements through strong Pt–S electron bridges; ii) the coordination role of surface S vacancies in Pt–Ni$_3$S$_2$/Co$_9$S$_8$–Sv regulates local electron structures between the Co/Ni and Pt sites. These two phenomena greatly boost HER catalytic activity and seawater electrolysis stability. This work provides a promising strategy for developing self-supported Pt SAs electrode with a high atom utilization efficiency and long-term stability for industrial seawater hydrogen evolution.

CRediT authorship contribution statement

Shanpeng Li: Writing – original draft, Methodology, Investigation, Formal analysis, Data curation, Conceptualization. **Yuling Zhuo:** Supervision, Formal analysis. **Dong Liu:** Writing – review & editing, Supervision, Formal analysis. **Hui Pan:** Writing – review & editing, Supervision, Formal analysis. **Zhenbo Wang:** Writing – review & editing, Supervision, Project administration, Funding acquisition, Formal analysis.

Declaration of Competing Interest

The authors declare that they have no known competing financial interests or personal relationships that could have appeared to influence the work reported in this paper.

Data Availability

Data will be made available on request.

Acknowledgements

Appendix A. Supporting information

Supplementary data associated with this article can be found in the online version at doi:10.1016/j.apcatb.2024.124188.

References

[1] Q. Ma, H. Jin, F. Xia, H. Xu, J. Zhu, R. Qin, H. Bai, B. Shuai, W. Huang, D. Chen, Z. Li, J. Wu, J. Yu, S. Mu, Ultralow Ru-assisted and vanadium-doped flower-like CoP/Ni$_2$P heterostructure for efficient water splitting in alkali and seawater, J. Mater. Chem. A 9 (2021) 26852–26860.

[2] S. Dresp, F. Dionigi, M. Klingenhof, P. Strasser, Direct electrolytic splitting of seawater: opportunities and challenges, ACS Energy Lett. 4 (2019) 933.

[3] Z. Chen, Y. Song, J. Cai, X. Zheng, D. Han, Y. Wu, Y. Zang, S. Niu, Y. Liu, J. Zhu, X. Liu, G. Wang, Tailoring the *d*-band centers enables Co$_4$N nanosheets to be highly active for hydrogen evolution catalysis, Angew. Chem. Int. Ed. 57 (2018) 5076–5080.

[4] L. Cao, Q. Luo, W. Liu, Y. Lin, X. Liu, Y. Cao, W. Zhang, Y. Wu, J. Yang, T. Yao, S. Wei, Identification of single-atom active sites in carbon-based cobalt catalysts during electrocatalytic hydrogen evolution, Nat. Catal. 2 (2019) 134–141.

[5] Y. Lei, Y. Wang, Y. Liu, C. Song, Q. Li, D. Wang, Y. Li, Designing atomic active centers for hydrogen evolution electrocatalysts, Angew. Chem. Int. Ed. 59 (2020) 20794–20812.

[6] W. Zhang, J. Zheng, X. Gu, B. Tang, B. Li, X. Wang, Facile synthesis, characterization and DFT studies of a nanostructured nickel–molybdenum–phosphorous planar electrode as an active electrocatalyst for the hydrogen evolution reaction, Nanoscale 11 (2019) 9353–9361.

[7] L. Zhang, L. Han, H. Liu, X. Liu, J. Luo, Potential-cycling synthesis of single platinum atoms for efficient hydrogen evolution in neutral media, Angew. Chem. Int. Ed. 56 (2017) 13694–13698.

[8] J.N. Tiwari, S. Sultan, C.W. Myung, T. Yoon, N. Li, M. Ha, A.M. Harzandi, H. J. Park, D.Y. Kim, S.S. Chandrasekaran, W.G. Lee, V. Vij, H. Kang, T.J. Shin, H. S. Shin, G. Lee, Z. Lee, K.S. Kim, Multicomponent electrocatalyst with ultralow Pt loading and high hydrogen evolution activity, Nat. Energy 3 (2018) 773–782.

[9] B. Qiao, A. Wang, X. Yang, L.F. Allard, Z. Jiang, Y. Cui, J. Liu, J. Li, T. Zhang, Single-atom catalysis of CO oxidation using Pt$_1$/FeO$_x$, Nat. Chem. 3 (2011) 634–641.

[10] A. Wang, J. Li, T. Zhang, Heterogeneous single-atom catalysis, Nat. Rev. Chem. 2 (2018) 65–81.

[11] N.J. O'Connor, A.S.M. Jonayat, M.J. Janik, T.P. Senftle, Interaction trends between single metal atoms and oxide supports identified with density functional theory and statistical learning, Nat. Catal. 1 (2018) 531–539.

[12] H. Fei, J. Dong, Y. Feng, C.S. Allen, C. Wan, B. Volosskiy, M. Li, Z. Zhao, Y. Wang, H. Sun, P. An, W. Chen, Z. Guo, C. Lee, D. Chen, I. Shakir, M. Liu, T. Hu, Y. Li, A. I. Kirkland, X. Duan, Y. Huang, General synthesis and definitive structural identification of MN$_4$C$_4$ single-atom catalysts with tunable electrocatalytic activities, Nat. Catal. 1 (2018) 63–72.

[13] Z. Chen, X. Li, J. Zhao, S. Zhang, J. Wang, H. Zhang, J. Zhang, Q. Dong, W. Zhang, W. Hu, X. Han, Stabilizing Pt single atoms through Pt−Se electron bridges on vacancy-enriched nickel selenide for efficient electrocatalytic hydrogen evolution, Angew. Chem. Int. Ed. 62 (2023) e202308686.

[14] K.L. Zhou, C. Wang, Z. Wang, C.B. Han, Q. Zhang, X. Ke, J. Liu, H. Wang, Seamlessly conductive Co(OH)$_2$ tailored atomically dispersed Pt electrocatalyst with a hierarchical nanostructure for an efficient hydrogen evolution reaction, Energy Environ. Sci. 13 (2020) 3082–3092.

[15] J. Wei, K. Xiao, Y. Chen, X.-P. Guo, B. Huang, Z.-Q. Liu, In situ precise anchoring of Pt single atoms in spinel Mn$_3$O$_4$ for a highly efficient hydrogen evolution reaction, Energy Environ. Sci. 15 (2022) 4592–4600.

[16] A. Pei, R. Xie, Y. Zhang, Y. Feng, W. Wang, S. Zhang, Z. Huang, L. Zhu, G. Chai, Z. Yang, Q. Gao, H. Ye, C. Shang, B.H. Chen, Z. Guo, Effective electronic tuning of Pt single atoms via heterogeneous atomic coordination of (Co,Ni)(OH)$_2$ for efficient hydrogen evolution, Energy Environ. Sci. 16 (2023) 1035–1048.

[17] Y. Shi, Z.-R. Ma, Y.-Y. Xiao, Y.-C. Yin, W.-M. Huang, Z.-C. Huang, Y.-Z. Zheng, F.-Y. Mu, R. Huang, G.-Y. Shi, Y.-Y. Sun, X.-H. Xia, W. Chen, Electronic metal–support interaction modulates single-atom platinum catalysis for hydrogen evolution reaction, Nat. Commun. 12 (2021) 3021.

[18] J. Zhang, Y. Zhao, X. Guo, C. Chen, C.-L. Dong, R.-S. Liu, C.-P. Han, Y. Li, Y. Gogotsi, G. Wang, Single platinum atoms immobilized on an MXene as an efficient catalyst for the hydrogen evolution reaction, Nat. Catal. 1 (2018) 985–992.

[19] S. Fang, X. Zhu, X. Liu, J. Gu, W. Liu, D. Wang, W. Zhang, Y. Lin, J. Lu, S. Wei, Y. Li, T. Yao, Uncovering near-free platinum single-atom dynamics during electrochemical hydrogen evolution reaction, Nat. Commun. 11 (2020) 1029.

[20] K.L. Zhou, C.B. Han, Z. Wang, X. Ke, C. Wang, Y. Jin, Q. Zhang, J. Liu, H. Wang, H. Yan, Atomically dispersed platinum modulated by sulfide as an efficient electrocatalyst for hydrogen evolution reaction, Adv. Sci. 8 (2021) 2100347.

[21] J. Zhu, Y. Tu, L. Cai, H. Ma, Y. Chai, L. Zhang, W. Zhang, Defect-assisted anchoring of Pt single atoms on MoS$_2$ nanosheets produces high-performance catalyst for industrial hydrogen evolution reaction, Small 18 (2022) 2104824.

[22] A. Mosallanezhad, C. Wei, P. Ahmadian Koudakan, Y. Fang, S. Niu, Z. Bian, B. Liu, T. Huang, H. Pan, G. Wang, Interfacial synergies between single-atomic Pt and CoS for enhancing hydrogen evolution reaction catalysis, Appl. Catal. B: Environ. 315 (2022) 121534.

[23] H. Su, S. Song, Y. Gao, N. Li, Y. Fu, L. Ge, W. Song, J. Liu, T. Ma, In situ electronic redistribution tuning of NiCo$_2$S$_4$ nanosheets for enhanced electrocatalysis, Adv. Funct. Mater. 32 (2022) 2109731.

[24] J. Chen, C. Chen, M. Qin, B. Li, B. Lin, Q. Mao, H. Yang, B. Liu, Y. Wang, Reversible hydrogen spillover in Ru-WO$_3$$_{-x}$ enhances hydrogen evolution activity in neutral pH water splitting, Nat. Commun. 13 (2022) 5382.

[25] X. Yang, F. Ling, J. Su, X. Zi, H. Zhang, H. Zhang, J. Li, M. Zhou, Y. Wang, Insights into the role of cation vacancy for significantly enhanced electrochemical nitrogen reduction, Appl. Catal. B: Environ. 264 (2020) 118477.

[26] Q. Wang, H. Xu, X. Qian, G. He, H. Chen, Sulfur vacancies engineered self-supported Co$_3$S$_4$ nanoflowers as an efficient bifunctional catalyst for electrochemical water splitting, Appl. Catal. B: Environ. 322 (2023) 122104.

[27] P. Yin, X. Luo, Y. Ma, S.-Q. Chu, S. Chen, X. Zheng, J. Lu, X.-J. Wu, H.-W. Liang, Sulfur stabilizing metal nanoclusters on carbon at high temperatures, Nat. Commun. 12 (2021) 3135.

[28] Q.-Q. Yan, D.-X. Wu, S.-Q. Chu, Z.-Q. Chen, Y. Lin, M.-X. Chen, J. Zhang, X.-J. Wu, H.-W. Liang, Reversing the charge transfer between platinum and sulfur-doped

carbon support for electrocatalytic hydrogen evolution, Nat. Commun. 10 (2019) 4977.

[29] C.-L. Yang, L.-N. Wang, P. Yin, J. Liu, M.-X. Chen, Q.-Q. Yan, Z.-S. Wang, S.-L. Xu, S.-Q. Chu, C. Cui, H. Ju, J. Zhu, Y. Lin, J. Shui, H.-W. Liang, Sulfur-anchoring synthesis of platinum intermetallic nanoparticle catalysts for fuel cells, Science 374 (2021) 459–464.

[30] L. Xiu, W. Pei, S. Zhou, Z. Wang, P. Yang, J. Zhao, J. Qiu, Multilevel hollow MXene tailored low-Pt catalyst for efficient hydrogen evolution in full-pH range and seawater, Adv. Funct. Mater. 30 (2020) 1910028.

[31] C. Wu, D. Li, S. Ding, Zu Rehman, Q. Liu, S. Chen, B. Zhang, L. Song, Monoatomic platinum-anchored metallic MoS$_2$: correlation between surface dopant and hydrogen evolution, J. Phys. Chem. Lett. 10 (2019) 6081–6087.

[32] D. Liu, X. Li, S. Chen, H. Yan, C. Wang, C. Wu, Y.A. Haleem, S. Duan, J. Lu, B. Ge, P. M. Ajayan, Y. Luo, J. Jiang, L. Song, Atomically dispersed platinum supported on curved carbon supports for efficient electrocatalytic hydrogen evolution, Nat. Energy 4 (2019) 512–518.

[33] S. Ye, F. Luo, Q. Zhang, P. Zhang, T. Xu, Q. Wang, D. He, L. Guo, Y. Zhang, C. He, X. Ouyang, M. Gu, J. Liu, X. Sun, Highly stable single Pt atomic sites anchored on aniline-stacked graphene for hydrogen evolution reaction, Energy Environ. Sci. 12 (2019) 1000–1007.

[34] Y. Yang, H. Yao, Z. Yu, S.M. Islam, H. He, M. Yuan, Y. Yue, K. Xu, W. Hao, G. Sun, H. Li, S. Ma, P. Zapol, M.G. Kanatzidis, Hierarchical nanoassembly of MoS$_2$/Co$_9$S$_8$/ Ni$_3$S$_2$/Ni as a highly efficient electrocatalyst for overall water splitting in a wide pH range, J. Am. Chem. Soc. 141 (2019) 10417–10430.

[35] J. Wen, S. Li, B. Li, Z. Song, H. Wang, R. Xiong, G. Fang, Synthesis of three dimensional Co$_9$S$_8$ nanorod@Ni(OH)$_2$ nanosheet core-shell structure for high performance supercapacitor application, J. Power Sources 284 (2015) 279–286.

[36] X. Feng, Q. Jiao, J. Zhang, H. Cui, H. Li, Y. Zhao, C. Feng, Integrating amorphous molybdenum sulfide nanosheets with a Co$_9$S$_8$@Ni$_3$S$_2$ array as an efficient electrocatalyst for overall water splitting, Langmuir 38 (2022) 3469–3479.

[37] H. Tan, B. Tang, Y. Lu, Q. Ji, L. Lv, H. Duan, N. Li, Y. Wang, S. Feng, Z. Li, C. Wang, F. Hu, Z. Sun, W. Yan, Engineering a local acid-like environment in alkaline medium for efficient hydrogen evolution reaction, Nat. Commun. 13 (2022) 2024.

[38] K. Jiang, B. Liu, M. Luo, S. Ning, M. Peng, Y. Zhao, Y.-R. Lu, T.-S. Chan, F.M.F. de Groot, Y. Tan, Single platinum atoms embedded in nanoporous cobalt selenide as electrocatalyst for accelerating hydrogen evolution reaction, Nat. Commun. 10 (2019) 1743.

[39] J. Li, P. Xu, R. Zhou, R. Li, L. Qiu, S.P. Jiang, D. Yuan, Co$_9$S$_8$–Ni$_3$S$_2$ heterointerfaced nanotubes on Ni foam as highly efficient and flexible bifunctional electrodes for water splitting, Electrochim. Acta 299 (2019) 152–162.

[40] H. Zhu, J. Zhang, R. Yanzhang, M. Du, Q. Wang, G. Gao, J. Wu, G. Wu, M. Zhang, B. Liu, J. Yao, X. Zhang, When cubic cobalt sulfide meets layered molybdenum disulfide: a core–shell system toward synergetic electrocatalytic water splitting, Adv. Mater. 27 (2015) 4752–4759.

[41] X. Zhou, X. Yang, M.N. Hedhili, H. Li, S. Min, J. Ming, K.-W. Huang, W. Zhang, L.-J. Li, Symmetrical synergy of hybrid Co$_9$S$_8$-MoS$_x$ electrocatalysts for hydrogen evolution reaction, Nano Energy 32 (2017) 470–478.

[42] F. Dvořák, M. Farnesi Camellone, A. Tovt, N.-D. Tran, F.R. Negreiros, M. Vorokhta, T. Skála, I. Matolínová, J. Mysliveček, V. Matolín, S. Fabris, Creating single-atom Pt-ceria catalysts by surface step decoration, Nat. Commun. 7 (2016) 10801.

[43] L. Lin, W. Zhou, R. Gao, S. Yao, X. Zhang, W. Xu, S. Zheng, Z. Jiang, Q. Yu, Y.-W. Li, C. Shi, X.-D. Wen, D. Ma, Low-temperature hydrogen production from water and methanol using Pt/α-MoC catalysts, Nature 544 (2017) 80–83.

[44] L. Wu, F. Zhang, S. Song, M. Ning, Q. Zhu, J. Zhou, G. Gao, Z. Chen, Q. Zhou, X. Xing, T. Tong, Y. Yao, J. Bao, L. Yu, S. Chen, Z. Ren, Efficient alkaline water/ seawater hydrogen evolution by a nanorod-nanoparticle-structured Ni-MoN catalyst with fast water-dissociation kinetics, Adv. Mater. 34 (2022) 2201774.

[45] N. Wen, D. Zhang, X. Zhao, X. Jiao, Y. Xia, D. Chen, Polarization manipulation of NiO nanosheets engineered with Fe/Pt single atoms for high-performance electrocatalytic overall alkaline seawater splitting, ACS Catal. 13 (2023) 7868–7878.

[46] K.L. Zhou, Z. Wang, C.B. Han, X. Ke, C. Wang, Y. Jin, Q. Zhang, J. Liu, H. Wang, H. Yan, Platinum single-atom catalyst coupled with transition metal/metal oxide heterostructure for accelerating alkaline hydrogen evolution reaction, Nat. Commun. 12 (2021) 3783.

[47] T.W. Hansen, A.T. DeLaRiva, S.R. Challa, A.K. Datye, Sintering of catalytic nanoparticles: particle migration or ostwald ripening? Acc. Chem. Res. 46 (2013) 1720–1730.

[48] Y. Dai, P. Lu, Z. Cao, C.T. Campbell, Y. Xia, The physical chemistry and materials science behind sinter-resistant catalysts, Chem. Soc. Rev. 47 (2018) 4314–4331.

[49] D. Liu, H. Ai, M. Chen, P. Zhou, B. Li, D. Liu, X. Du, K.H. Lo, K.-W. Ng, S.-P. Wang, S. Chen, G. Xing, J. Hu, H. Pan, Multi-phase heterostructure of CoNiP/Co$_x$P for enhanced hydrogen evolution under alkaline and seawater conditions by promoting H$_2$O dissociation, Small 17 (2021) 2007557.